Check for updates

Optoelectronic properties of Ag$_2$S/graphene and FeS$_2$/graphene nanostructures and interfaces: A density functional study including dispersion forces

Javier Amaya Suárez[1], Cristina García-Prieto[1], M. Dolores Fernández-Martínez[1], Elena R. Remesal[1], Antonio M. Márquez[1], Javier Fernández Sanz[1,a)]

[1] *Departamento de Química Física, Facultad de Química, Universidad de Sevilla, 41012 Seville, Spain*
a) Address all correspondence to this author. e-mail: sanz@us.es

The optoelectronic properties of several Ag$_2$S/graphene and FeS$_2$/graphene nanostructures are examined through density functional theory calculations including dispersion forces. First, we analyzed the electronic structure of Ag$_2$S and FeS$_2$ nanocluster models, as prototypes of quantum dots, focusing on the electronic structure and absorption spectra. In the case of FeS$_2$ nanoparticle, both ferro- and antiferromagnetic arrangements were considered. Then, Ag$_2$S and FeS$_2$ nanoclusters were adsorbed on top of both graphite and graphene slab models to study the stability of the systems as well as the effect of the nanocluster–surface interaction in the electronic structure, including an insight into the electron injection mechanisms in these systems. Finally, interface models, consisting of Ag$_2$S or FeS$_2$ thin films adsorbed on a graphene layer, were built and their optoelectronic properties examined. Overall, the results obtained in this work, support the suitability of these systems for their usage in solar cells.

Introduction

The Sun is an inexhaustible clean energy source. It has heated the Earth, driven the wind and risen the ocean waves for millions of years, and many more to come. Among all the ways that we can use the energy produced by the Sun, photovoltaics (PVs) seems to be one of the most promising technology for the upcoming years [1].

A solar cell is a device that absorbs sunlight and produces a direct current. This cell is based on a p–n junction, which consists of a doped semiconductor material having an excess of holes (p), or electrons (n) in each side. The efficiency of such device depends on various factors like (a) the efficiency of light absorption; (b) an effective charge separation and (c) fast transport and recollection of the charge carriers. The Shockley–Queisser limit marks the theoretical upper limit of the efficiency of a PV device based on a p–n junction to be 33.7% [2].

During the last decades, solar cells have been developed in such a way that it is possible to distinguish three different generations of them nowadays [3]. The first generation encompasses single crystal and polycrystalline silicon-based cells, which represent about 90% of the global market. The second generation, called thin-film solar cells, consists basically of thin layers of various materials joined together forming a multijunction which can, theoretically, overcome the Shockley–Queisser limit [4]. Development of nanotechnology since the 1990s made it possible for a new generation of solar cells to emerge, focusing on using the enhanced optoelectronic properties displayed by nanostructures to push the efficiency boundaries as well as using more environmentally friendly chemical compounds as light harvesters [5].

Among the technologies found in the third-generation PVs, quantum dot (QD) sensitized solar cells (QDSCs) are one of the most promising technologies [6–8]. QDs are nanoparticles (NPs) made of a semiconductor material that are small enough to exhibit quantum confinement effects such as multiple exciton generation, MEG [9], size-dependent bandgaps [10] and large absorption coefficients [11]. Besides solar cells, technological applications for QDs include fluorescent labeling of biological systems [11–13], quantum computing [14], lasers [15] and LEDs [16]. Due to the MEG, QDSCs are theoretically able to overcome the Shockley–Queisser limit to reach a limit efficiency of 42% [17]. In these cells, QDs are adsorbed onto a wide-gap

mesoporous semiconductor material like TiO_2 or ZnO [7], that is able to accept the excited electrons produced in the QD due to light absorption.

Because of the outstanding mechanical, thermal and optoelectronic properties displayed by graphene, it has become a very attractive material for various technological applications in the last years [18–21]. Its performance assuming various roles in QDSCs, such as electrolyte, electrode, sensitizer and transparent conductor, have been tested recently yielding promising results [22]. Additionally, graphene interfacing with a large diversity of materials is deserving much attention today. In particular, metal sulfides, like MoS_2 or VS_2, have been adsorbed onto graphene for different applications [23, 24]. Structures consisting of a monolayer or few-layer interfaces have been considered. These nanostructures exhibit a variety of exotic mechanical and electronic properties making them of interest in several high-tech scenarios [25–28].

Silver sulfide, Ag_2S, is a promising material for electronic devices. It has deserved considerable attention due to its good stability, low toxicity and electronic properties such as large absorption coefficient, a direct bandgap of about 1.0 eV, which is close to the theoretical optimal value of 1.13 eV [29], and an optical absorption range 2 to 4 times wider than those of the widely used CdS and CdSe [30]. Such properties make silver sulfide an attractive material for QDSCs [31–34].

Iron pyrite, FeS_2, is another interesting candidate for PV applications due to its high abundancy, non-toxicity, long carrier diffusion length and bandgap value of 0.95 eV [35]. Nevertheless, despite showing large photocurrent values, the low open-circuit potential, V_{OC}, shown by FeS_2 thin-film solar cells, causes overall efficiencies to drop [36–39]. The electronic structure of FeS_2 has been subject of intensive research, both experimentally [40–44] and theoretically in the last years [45–50]. While in bulk, FeS_2 has been identified as a non-magnetic material with divalent, low-spin Fe atoms. Nonetheless, the most stable (001) surface was shown to be spin-polarized and with a high concentration of defects, which could explain the low efficiencies, shown. FeS_2 nanostructures of different sizes have been previously synthesized and tested as possible light harvesters for photovoltaic applications [51–54]. In the case of Ag_2S, NPs deposited on graphene nanosheets have been synthetized, and its properties as selective chemical sensor and supercapacitors considered [55, 56]. With respect to Fe_2S/graphene films, their potential to behave as counter electrodes in dye-sensitized solar cells has been considered [57].

In the present work, we explore theoretically the structural and optoelectronic properties of different Ag_2S and FeS_2 nanostructures and its interaction with a graphene layer in view of its application as light captors in solar cells. First, the interaction of two silver sulfide and one iron pyrite cluster with graphite and graphene surfaces was examined. Then, more

complex models consisting of two stoichiometric monolayers of silver sulfide and one of iron pyrite, which correspond to different surface planes epitaxially adsorbed on graphene, were developed. The nature of surface–surface interactions was carefully analyzed and the optoelectronic properties of these heterostructures were simulated. All the calculations subtending the theoretical approach were made within the framework of the density functional theory (DFT), using the generalized gradient approximation (GGA) and including van der Waals contributions.

Results and discussion

Isolated nanoparticles

Ag_2S

To model Ag_2S QDs of an adequate size with a reasonable computational cost, two different $(Ag_2S)_n$ nanocluster geometries with $n = 4, 5$ were selected from the work by He et al. [58]. Fig. 1a shows the atomic arrangement of these clusters. Calculated Ag–S bond distances are slightly shorter for the apical bonds (2.38–2.46 Å) than for the equatorial bonds (2.45–2.51 Å) except for the protruding Ag atom in $Ag_{10}S_5$ that presents a longer Ag–S distance of 2.76 Å. Bader charges were calculated for the model NPs, yielding similar results regardless of the selected geometry, with mean charges of $+ 0.306$ and $- 0.613$ e^- for Ag and S atoms respectively. These values are consistent with the difference of electronegativity existing between the two elements, as well as the Ag_2S stoichiometry, resulting in the S atoms showing charges twice (and opposite sign) of those of Ag atoms to maintain electroneutrality but the computed values indicate a large covalent contribution to the bond. The electronic structure of both models was examined by means of the density of states (DOS) and electronic absorption spectra $[\varepsilon_2(\omega)]$. Focussing on the Ag_8S_4 electronic levels are distributed in three different energy regions close to the Fermi level (see Fig. S1 in Supplementary Information). From $- 5$ to $- 2$ eV, a first group of states, corresponding almost entirely to Ag (4d) electronic levels; a second group, between $- 1.8$ and 0 eV, can be assigned to both Ag (4d) and S (3p) levels. Due to the almost equitable contribution of both elements to these states, this region can be interpreted as the covalent contribution to the Ag–S bond. Finally, above 1.15 eV, empty states corresponding to both Ag and S atoms compose the conduction states. A similar profile can be found for the $Ag_{10}S_5$ nanocluster but, in this case, the LUMO is located at 0.8 eV while the remaining empty states are placed beyond 2.5 eV. This distribution of the electronic states correlates with that of Ag_2S bulk found in previous studies using pure GGA and hybrid methodologies that also obtain a substantial mixing of Ag and S states in the valence band [31].
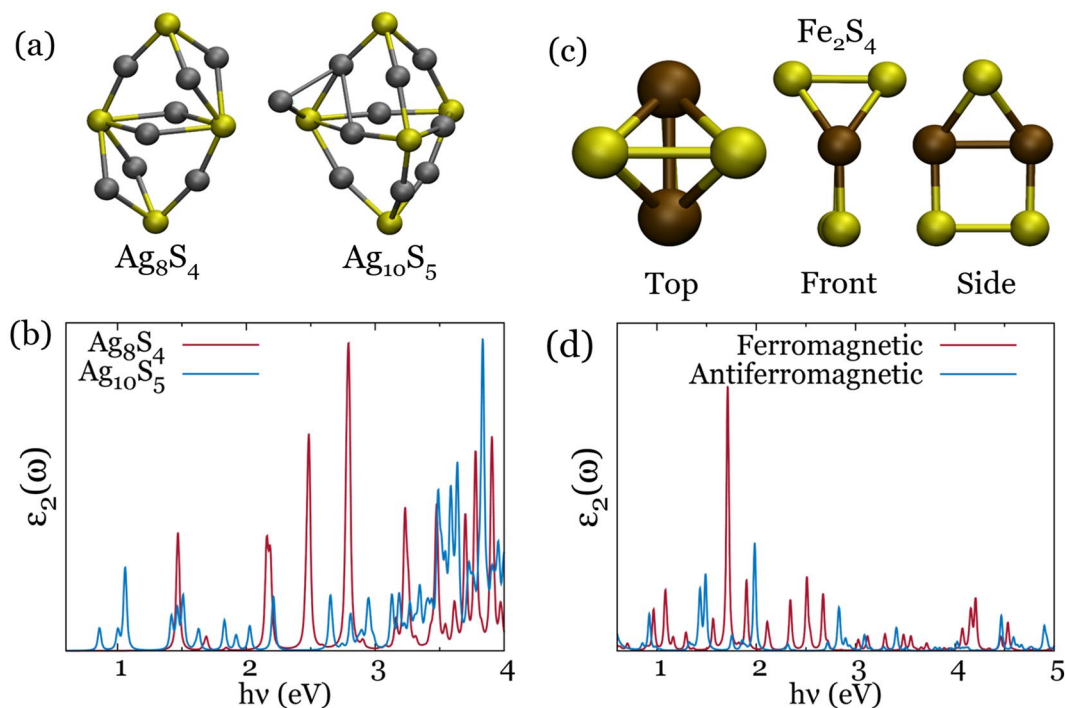
Figure 1: (a) $(Ag_2S)_n$ nanoparticles geometries. Colors: Ag, gray; S, yellow, (b) absorption spectra for the $(Ag_2S)_n$ nanoclusters. (c) Fe_2S_4 nanocluster geometry. Colors: Fe, ochre; S, yellow, (d) absorption spectra for both magnetic arrangements.

Figure 1b shows the absorption spectra obtained for the cluster models. For Ag_8S_4, a well-defined profile is found, showing optical activity in the UV–Vis range with a first absorption maximum located at 1.5 eV and a global maximum about 2.8 eV. In the case of $Ag_{10}S_5$, a red shift is produced in the absorption due to the reduction of the bandgap. Its first peak can be observed at 0.8 eV and a global maximum located at 3.8 eV, in the UV region.

FeS$_2$

For FeS_2 NPs, a nanocluster consisting of two Fe atoms and two S_2 dimers were obtained from the bulk system. This cluster was selected due to the possibility of studying different magnetic arrangements of the iron atoms in a system with an associated low computational cost. Figure 1c shows different views of the geometry of the selected nanocluster. Both ferromagnetic and antiferromagnetic states were calculated for the nanocluster. While Fe–S bond distances are similar in both magnetic arrangements (2.12–2.13 Å at the bottom and 2.19–2.22 Å at the top), the Fe–Fe distance is significantly shorter (2.41 Å) in the antiferromagnetic state than in the ferromagnetic one (2.50 Å). This can be understood looking at the relative energies obtained, Bader charges, and magnetization for the Fe atoms for both magnetic states presented in Table 1. The ferromagnetic spin arrangement is shown to be more stable by 0.160 eV, with Fe atom charges about 0.9 |e| and magnetization values around

TABLE 1: Relative energies (E_{rel}), Bader charge (q) and magnetization (M) for the Fe atoms and Fe_2S_4 cluster in ferromagnetic and antiferromagnetic states.

State	E_{rel} (eV)	q Fe	M Fe (μ_B)	M cluster (μ_B)
Ferro-	0	0.922	2.591	5.279
Antiferro-	0.160	0.963	±2.459	0.000

2.6 μ_B. In the case of the antiferromagnetic arrangement while Bader charge values for the Fe atoms are close to those found on the ferromagnetic cluster, magnetization of the Fe atoms is slightly smaller ~ 2.46 μ_B. Those different magnetic states do not only modify the electronic structure of the NP, but they also have a significant influence in the geometry, as the Fe atoms tend to get closer to each other in the ferromagnetic disposition as previously indicated.

As for the $(Ag_2S)_n$ clusters, the electronic structure of the Fe_2S_4 NP was studied focussing on the DOS and absorption spectra. The DOS profiles (see Fig. S2 in Supplementary Information) obtained for both the ferro- and antiferromagnetic states show a similar discrete-level distribution with a valence band mainly formed by a mix of Fe (3d) and S (3p) states, indicative of a substantial covalent contribution to the bonding. Main differences in DOS are found in the HOMO–LUMO value ($E_{HOMO–LUMO}$), with values of 0.095 eV and 0.340 eV for the ferro- and antiferromagnetic spin arrangements, respectively. Figure 1d shows the absorption spectra obtained for both

magnetic states. It is worth noting that both systems show optical activity in a wide range of energies, including the UV–Vis region, located around 1.5–4.0 eV. For the magnetic NP, a first absorption maximum can be observed at 0.37 eV with another maximum at 1.40 eV, inside the near-infrared region. In the case of the antiferromagnetic state, the first peak emerges at 0.49 eV showing a second maximum at 1.80 eV, inside the visible region of the electromagnetic spectrum. Additionally, it can be observed that the peaks for the ferromagnetic cluster are located at lower energies than those of the antiferromagnetic NP in agreement with the lower HOMO–LUMO gap obtained for the ferromagnetic system.

Nanoparticle adsorption on graphene and graphite

$(Ag_2S)_n$ adsorption

In the $(Ag_2S)_n$-surface models, nanoclusters have been linked to the surface via Ag atoms due to the partial positive charge that these atoms present in gas phase cluster models, as discussed in the previous section. This is expected to be the most favorable form of adsorption given the negative-charged π electronic cloud located on top of both graphene and graphite. With the goal of avoiding undesired interactions between the different cluster images, dimensions for the substrate models are 19.68 Å × 17.05 Å, including 128 carbon atoms for graphene and 512 for the graphite model, which includes four single atom layers. A top view of the Ag_8S_4/graphene model can be observed in Fig. 2a. To measure the adsorption strength, interaction energy, E_{ads}, is defined as:

$$E_{ads} = E_{NP+surf} - E_{NP} - E_{surf}, \tag{1}$$

where $E_{NP+surf}$ is the total energy of the system where $(Ag_2S)_n$ nanocluster is adsorbed on either graphene or graphite, E_{NP} is the energy of the isolated NP in gas phase and E_{surf} is the energy of the clean graphene or graphite surfaces. With this definition, negative values imply stabilizing interactions.

Table 2 shows adsorption energy values obtained for the $(Ag_2S)_n$ adsorption on graphene and graphite. First of all, we see that the interaction with graphite is larger than with graphene, whatever the cluster is. Also, in both surfaces, the binding energy
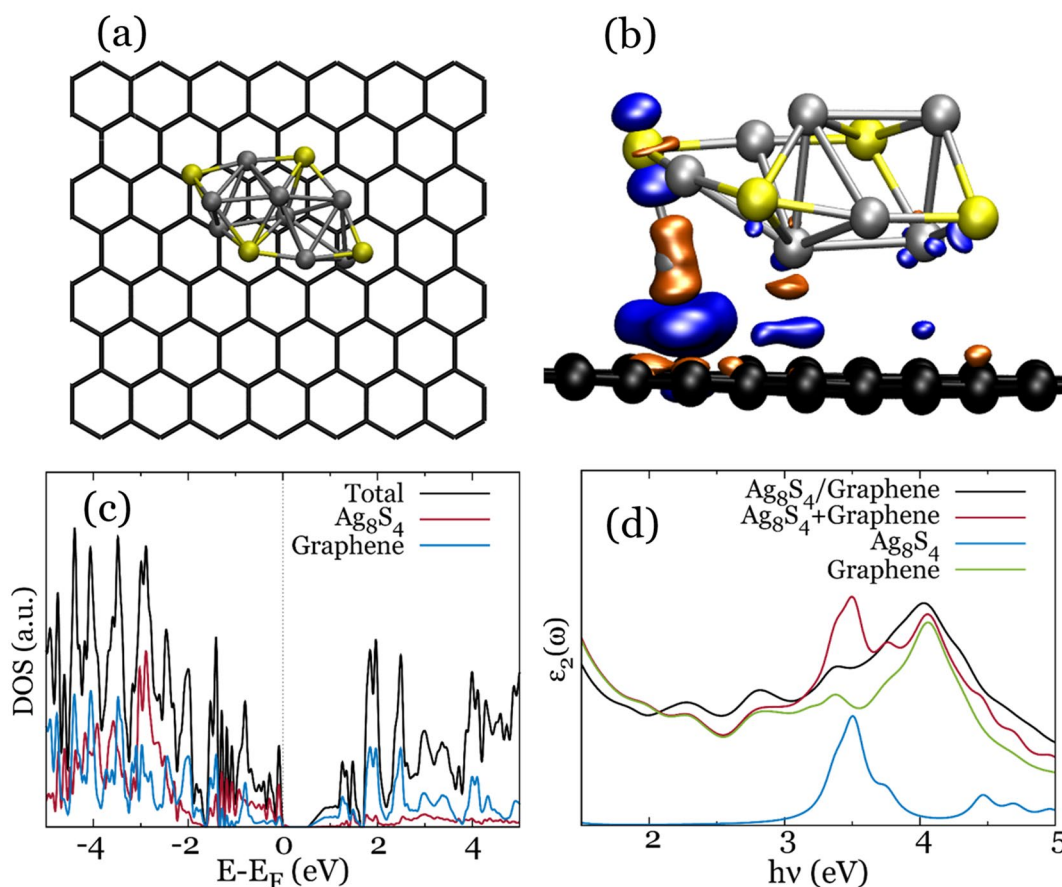
Figure 2: Main features for the Ag_8S_4/graphene model. (a) Top view of the geometry. Colors: Ag, gray; S, yellow; C, black. (b) Electron density difference map. Orange (blue) regions imply a decrease (increase) in electron density. Isovalue is set to ± 0.01. (c) Total and partial DOS. Fermi level is set to zero. (d) Absorption spectra including isolated fragments.

TABLE 2: Adsorption energies (E_{ads}) and Ag–C bond distances for the nanocluster/substrate models.

System	PBE		PBE-TS	
	E_{ads} (eV)	Ag–C bond (Å)	E_{ads} (eV)	Ag–C bond (Å)
Ag_8S_4/graphene	− 1.04	2.42	− 2.10	2.41
Ag_8S_4/graphite	− 1.53	2.39	− 2.58	2.39
$Ag_{10}S_5$/graphene	− 0.04	3.31	− 1.24	2.82
$Ag_{10}S_5$/graphite	0.39	3.11	− 1.63	2.76

of Ag_8S_4 NP is about 1 eV larger than that of $Ag_{10}S_5$ cluster. The effect of dispersion forces is quite significant, increasing adsorption energies by about 1.0–1.3 eV. At the same time, the Ag–C bond length is shorter in the case of the Ag_8S_4 NP (∼ 2.4 Å) than for the $Ag_{10}S_5$ cluster (∼ 2.8 Å) in both surfaces. These differences can be explained by the cluster geometry. While Ag_8S_4 adsorbs through a silver atom located at the edge of the NP (see Fig. 2a, b), which is more flexible, $Ag_{10}S_5$ must interact with the surface through a less flexible silver atom located at the center of the nanocluster. Furthermore, this geometry implies a repulsive interaction between the graphene π-electron cloud and the large electronic clouds of the S atoms of the cluster that are first neighbors to the cluster Ag atom.

To analyze the bond created between the nanocluster and graphene layer, Fig. 2b shows the electron density difference regions represented with an isovalue of ± 0.01 |e⁻| Å⁻³ for the Ag_8S_4/graphene system. A charge redistribution can be seen between the graphene sheet and the silver atom closest to the substrate, indicating the formation of a chemical bond. There is an increase of electron density on the region between the cluster silver atom and the graphene surface that is related to a clear repolarization of the charge density on the Ag atom but also to a displacement of some electron density of the π-cloud of the graphene sheet. Bader charges analysis reveals a net charge transfer of 0.081 e⁻ to the NP from the graphene sheet. This bonding mechanism (small charge transfer from the surface to the NP) help us to understand the smaller binding energies found for the NP/graphite systems: the formation of graphite implies the displacement of electron density of the C-monolayers to the interlayer space to allow for the formation of the π-electron cloud between the C-layers. In turns, this reduces the electron density at the top of the graphite surface available for the formation of the bond with the $(AgS_2)_n$ NP.

DOS for the Ag_8S_4/graphene model is shown in Fig. 2c. The first point to notice is the opening of a 0.6 eV gap in the graphene electronic structure, resulting in the disappearance of the graphene Dirac cone. Two main bands can be observed: the valence band, from − 5 to 0 eV that can be projected to both cluster and graphene sheet levels and the conduction band, beyond 0.6 eV is mainly located on the graphene substrate with

cluster levels located above 1.1 eV, which is consistent with the HOMO–LUMO gap value from the isolated nanocluster. Finally, Fig. 2d shows the calculated absorption spectra for the Ag_8S_4/graphene system, as well as those of its isolated fragments and the sum of them. This decomposition allows us to analyze the electron injection mechanism present in the system.

Electron injection mechanisms can be distinguished analysing the energy of the bands in the absorption spectra [32, 59–61]. On the one hand, an indirect injection mechanism means the promotion of an electron from a valence state to a conduction state, both belonging to the NP, followed by an injection of the excited electron from the NP conduction state to the empty states of the graphene. This mechanism implies absorption energies like those of the isolated NP. On the other hand, a direct injection mechanism produces an excitation directly from the NP valence states to the graphene conduction states. This mechanism requires a lower energy than the indirect mechanism, resulting a red shift in the energy bands shown in the absorption spectra.

Back to Fig. 2d, optical activity can be observed in the UV–Vis region for all the systems plotted, with the graphene layer showing a greater activity than the NP due to the high ratio of carbon atoms per silver and sulfur atoms in the system. It can be observed that the calculated Ag_8S_4/graphene spectrum is like that of the sum of Ag_8S_4 and graphene (Ag_8S_4 + graphene). However, a non-minor contrast is found at energies around 3.5 eV, where the isolated NP is shown to have its maximum absorption. This leads to a local maximum that is shown in the Ag_8S_4 + graphene spectrum but not in Ag_8S_4/graphene. This feature, in addition to the absorption increment observed in the range from 2 to 3 eV, is characteristic of the direct injection mechanism. Besides this, the similarity of both spectra in all other energy ranges, provides evidence of the indirect injection mechanism. So, it is fair to conclude that the injection mechanism is not unique in any case, and that a mixture of both is expected.

The $Ag_{10}S_5$/graphene system was studied in a similar way to Ag_8S_4/graphene. Figure S3 in Supplementary Information shows the geometry of the system, with the NP adsorbed in the middle of a layer of graphene consisting of 128 carbon atoms. Results are like those discussed in the Ag_8S_4/graphene system. The electron density difference maps show an increase of the electron density in the region between the cluster Ag atom and the graphene sheet related to a repolarization of the π-electron cloud and to a charge transfer of 0.038 e⁻ from the graphene to the NP. The analysis of the DOS is also similar, but in this case the gap is only 0.3 eV wide as can be expected from the lower interaction between the nanocluster and the graphene sheet. The calculated adsorption spectrum shows a high intensity band at ∼ 0.26 eV, consistent with the computed gap, that can be argued as a clear indication of a direct injection mechanism. At the same time, some adsorption peaks hold their positions with respect to the

isolated system. So, as in the Ag$_8$S$_4$/graphene system, both injection mechanisms operate at the same time.

Fe$_2$S$_4$ adsorption

To analyze the interaction between the Fe$_2$S$_4$ nanocluster and the graphene layer, a graphene model consisting of 32 carbon atoms was selected due to its affordable computational cost as well as allow a distance between nanocluster images of at least 6 Å. A total number of 32 different adsorption geometries were tried in which the interaction occurs along either a Fe or S atom, with the iron atoms been ferromagnetic or antiferromagnetically coupled and adsorbing in a top, bridge or hollow position onto the carbon support. Adsorption energy, E_{ads}, was calculated for these systems according to Eq. 1 shown previously for the (Ag$_2$S)$_n$ NPs adsorption. The most stable geometry, as can be observed in Fig. 3a,b, shows the interaction between the nanocluster and the support happening through one of the Fe atoms adsorbed in a hollow position, in other words, at the center of a six-carbon hexagon forming the graphene honeycomb mesh. Additionally, for the

most stable structure, an antiferromagnetic state was found for the iron atoms, giving an E_{ads} value of -2.127 eV.

Calculated Bader charges for the two Fe atoms (0.859 and 0.932), shows lower values to those of the isolated antiferromagnetic nanocluster (0.963), meaning that an electronic reorganization inside the cluster is taking place. Values for the magnetization for both iron atoms as well as the Fe$_2$S$_4$/graphene system show the antiferromagnetic state of the iron atoms ($+0.989$ μ_B and -0.721 μ_B) as well as the low value obtained for the whole system (0.102 μ_B). Bader charges show, as expected, a large electronic reorganization with a net charge transfer of 0.408 e$^-$ taking place, in this case from the nanocluster to the graphene layer. Figure 3b shows the reorganization of the electronic density in the system due to the cluster adsorption representing the electron density difference regions with isovalues of ± 0.01 $|e^-|$ Å^{-3}. In this representation, which gives us an insight into the chemical bond creation between these two systems, a large redistribution is observed in the area surrounding the adsorbed Fe atom and the six surface neighbor C atoms, associated to the
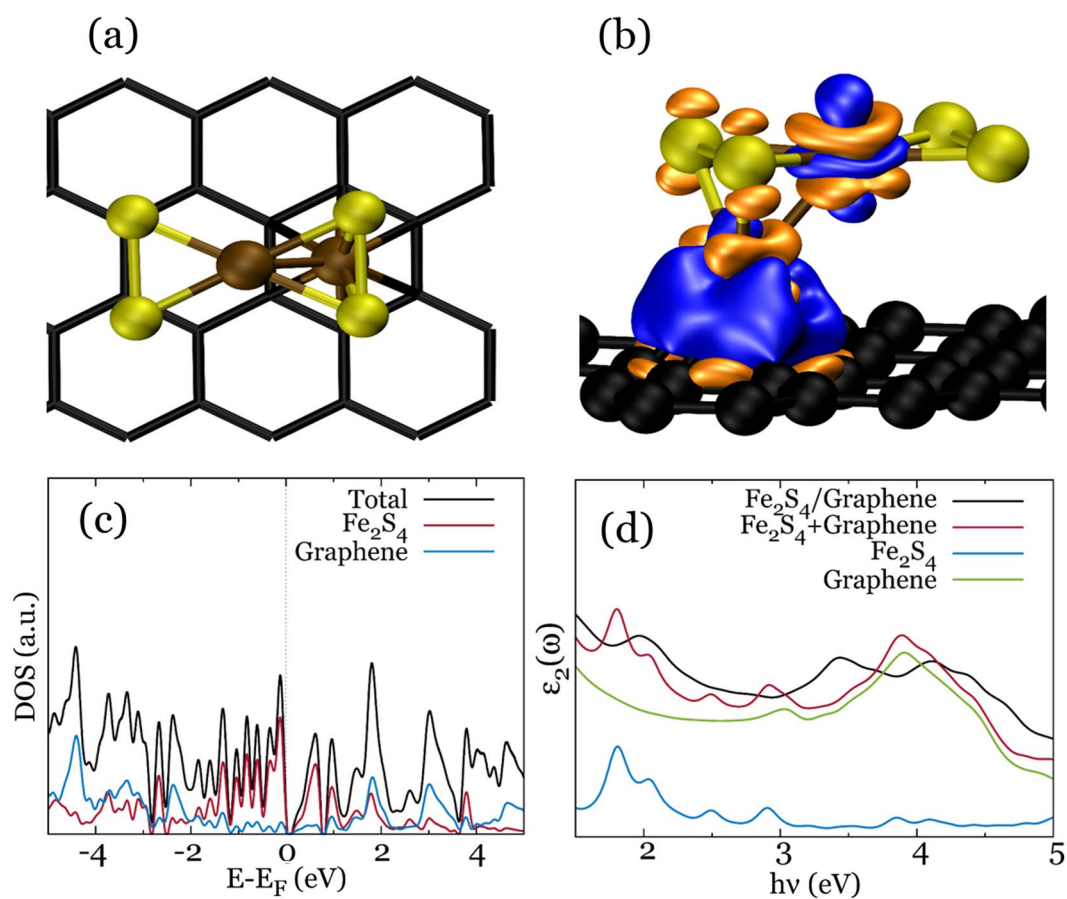
Figure 3: Main features for the Fe$_2$S$_4$/graphene model. (a) Top view of the geometry. Colors: Fe, ochre; S, yellow; C, black. (b) Electron density difference map. Orange (blue) regions imply a decrease (increase) in electron density. Isovalue is set to ± 0.01. (c) Total and partial DOS. Fermi level is set to zero. (d) Absorption spectra including isolated fragments.

large binding energy computed for this system. Additionally, some reorganization of the electron density is also observed in the second Fe atom.

Figure 3c shows the obtained total and partial DOS for the Fe$_2$S$_4$/graphene system. As in the case of the (Ag$_2$S)$_n$/graphene systems, the conduction band, located above 0.135 eV, which is the bandgap value calculated for this system, appears to have similar partial contribution of both the nanocluster and the graphene layer in the majority of the energy values shown, except for those close to the Fermi level, where the NP contribution is shown to be predominant. The obtained absorption spectra for the Fe$_2$S$_4$/graphene system, its components and the Fe$_2$S$_4$ + graphene sum is shown in Fig. 3d. In general terms, nanocluster adsorption enhances the optical activity of the system, while shifting some of the absorption bands and showing a moderate absorption through the UV–Vis region. Local maxima can be found at energies around 2 eV, 3.5 eV and 4.2 eV, which comparing with the Fe$_2$S$_4$ + graphene representation, can help us understand the electron injection mechanisms present on the system. The enhanced activity shown by the Fe$_2$S$_4$/graphene system at most of the energies studied, can be an indicative of a direct injection mechanism as the band position tend to red shift. Also, the similarity of both spectra in terms of the local curvature of the graphs,

can be interpreted as a proof of the presence of the indirect injection mechanism.

Thin films interaction with graphene

Ag$_2$S thin film/graphene structure

In order to model the interaction between the Ag$_2$S thin film and the graphene layer, two different slab models were constructed from acanthite structure (α-Ag$_2$S) considering two different surfaces, (100) and (010) as shown in Figs. 4a, b and 5a, b. Surface models dimensions (Table 3) were selected to account for the minimum possible mismatch while maintaining an affordable computational cost.

To measure the adsorption strength, adsorption energy, E_{ads}, is defined as:

$$E_{ads} = \frac{E_{tf+gr} - E_{tf} - E_{gr}}{A}, \qquad (2)$$

where E_{tf+gr} is the total energy of the system where semiconductor thin film is adsorbed on grapheme, E_{tf} is the energy of the isolated thin film, E_{gr} is the energy of the clean graphene surface, and A is the surface area of the interface between the two materials. With this definition, negative values imply stabilizing interactions. Table 4 shows the obtained E_{ads} values for the
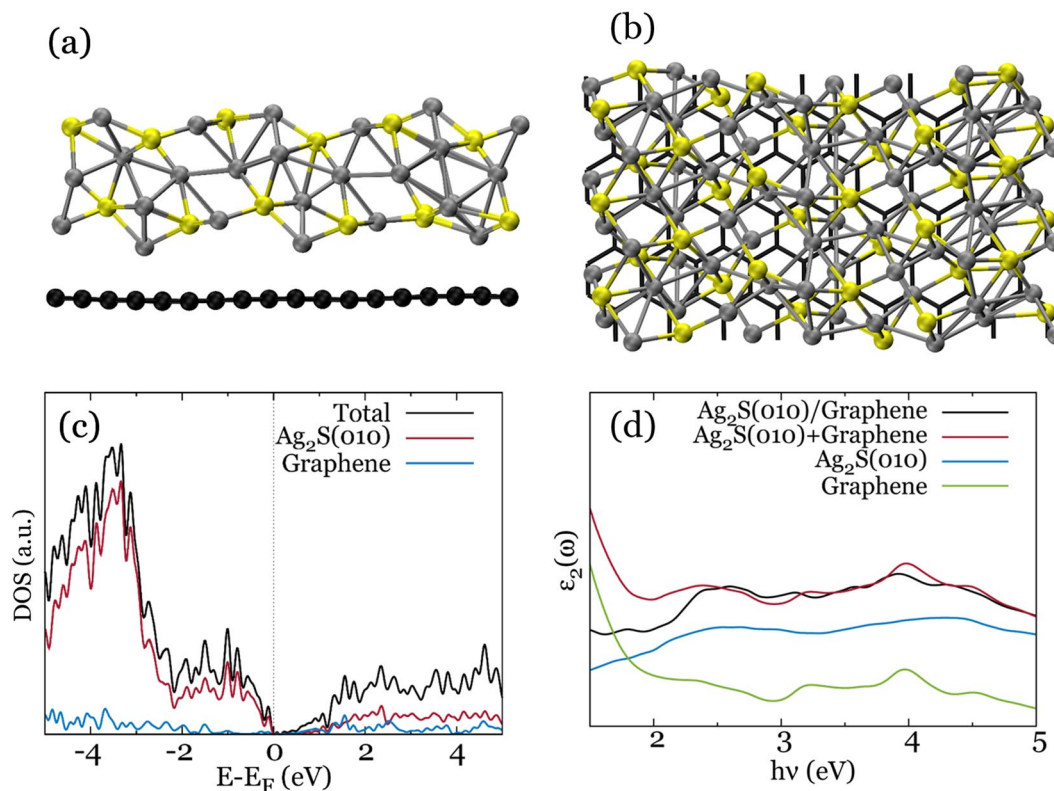
Figure 4: Main features for the Ag$_2$S(010)/graphene model. (a) Side and (b) top view of the geometry. Colors: Ag, gray; S, yellow; C, black. (c) Total and partial DOS. Fermi level is set to zero. (d) Absorption spectra including isolated fragments.
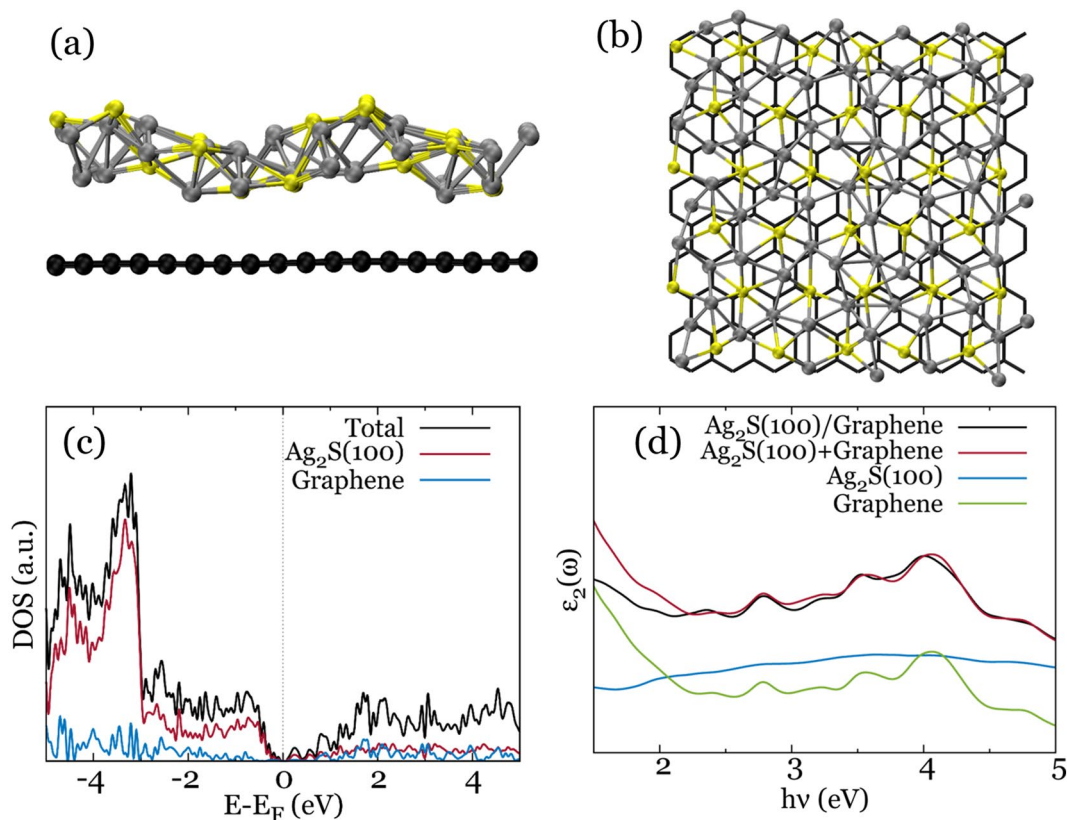
Figure 5: Main features for the Ag₂S(100)/graphene model. (a) Side and (b) top view of the geometry. Colors: Ag, gray; S, yellow; C, black. (c) Total and partial DOS. Fermi level is set to zero. (d) Absorption spectra including isolated fragments.

TABLE 3: Dimensions and mismatch for the semiconductor thin film/graphene models.

Semiconductor surface	Thin film model (Å²)	Graphene model (Å²)	Mismatch (%)
$Ag_2S(010)$	$a \times c$ (12.8×22.5)	22.1×12.8	1.1
$Ag_2S(100)$	$b \times c$ (20.9×22.5)	22.1×21.3	0.5
$FeS_2(100)$	$a \times b$ (16.1×16.1)	17.0×17.2	6.1

TABLE 4: Adsorption energy (E_{ads}) and slab distances for the semiconductor thin film/graphene and graphene/graphene models.

Model	E_{ads} (J/m²)	Slab distances (Å)
$Ag_2S(010)$/graphene	−0.47	2.5
$Ag_2S(100)$/graphene	−0.31	3.1
$FeS_2(100)$/graphene	−0.46	3.4
Graphene/graphene	−0.50	3.3

Ag_2S thin film/graphene models. It can be observed that Ag_2S thin films present moderately strong adsorption to the graphene sheet, with values close to the grapheme–graphene interaction in graphite. Slab distances are also listed on Table 4, showing that Ag_2S thin film–graphene distances are similar or even shorter than the spacing between atomic layers in graphite.

Total and partial DOS obtained for the $Ag_2S(010)$/graphene system are showed in Fig. 4c. The valence band located above − 5 eV, is mainly assigned to the Ag_2S electronic states, and the conduction band that appears just before the Fermi level. A metallic behavior is found for this system, as the calculated bandgap value is zero. This is mainly due to the graphene layer that is known to be a zero-gap system when isolated while the $Ag_2S(010)$ thin film has a gap value of 0.35 eV. However, mixing of electronic states is observed when the interface is created, leading to some contribution of Ag_2S levels in the conduction states close to the Fermi level. The thin film–graphene interaction is substantiated also by a large net charge transfer of 0.24 $|e^-|/nm^2$ from the semiconductor thin film to the graphene support obtained from the Bader charge analysis. Figure 4d shows the calculated absorption spectra for the $Ag_2S(010)$/graphene system, as well as those of its components and the sum of them.

All spectra show optical activity in the UV–Vis region, with local maxima located around 2.4 eV and 4 eV, while a good match between the $Ag_2S(010)$/graphene and $Ag_2S(010)$ + graphene can be observed. This is a clear indication of a major contribution of the indirect electron injection mechanism in this system.

The distances and binding energies computed for the $Ag_2S(100)$ thin film and the graphene sheet indicate that the interaction in this layered system is weaker than in the $Ag_2S(101)$/graphene system. The interlayer distances increase to 3.1 Å and, more significative, the adsorption energy decreases to -0.31 J/m^2, nearly half the value found between the atomic layers of graphite. This low interaction is also reflected in a much lower charge transfer of only 0.024 $|e^-|/nm^2$ from the graphene to the $Ag_2S(100)$ thin film. In this system DOS (see Fig. 5c), the valence band, that extends from -5 eV to the Fermi level, is composed almost completely of Ag_2S electronic states. After a short bandgap value of 0.05 eV the conduction band, which can be projected to both Ag_2S and graphene levels, follows. The absorption spectra (Fig. 5d) for the $Ag_2S(100)$/graphene system, shows maxima absorption peaks at energies around 2.8 eV, 3.5 eV and 4 eV, which can be correlated with those of the graphene layer. A high correlation can also be observed for the $Ag_2S(100)$/graphene and $Ag_2S(100)$ + graphene spectrum,

which is an indication of a majority contribution of the indirect electron injection mechanism in this system.

FeS$_2$ thin film/graphene

Finally, we explored the absorption of a FeS_2 monolayer on graphene. The $FeS_2(100)$ surface was selected because it is known to be most stable, as it presents the minimal value of surface energy [62, 63]. To model this system, a single slab model of the $FeS_2(100)$ surface was selected, containing 18 Fe and 36 S atoms, as well as a graphene sheet with 112 carbon atoms. Dimensions of the two systems are presented in Table 3, where it is shown that the FeS_2 model sizes are 16.1×16.1 Å, while the graphene dimensions are 17.0×17.2 Å, yielding a mismatch between the lattice parameters of 6.1%. Geometry for this system is shown in Fig. 6a, b.

Adsorption energy for this system was calculated to be -0.46 J/m^2 as shown in Table 4. This value, which is similar to that obtained for the $Ag_2S(010)$/graphene system (-0.47 J/m^2), implies a good structural stability for this system as it is found to be also very close to the graphene/graphene value (-0.50 J/m^2), that represent the graphite crystal. Table 4 also shows the distances between these two layers to be 3.4 Å which is also a very consistent value compared to the 3.3 Å observed between graphene layers in graphite.
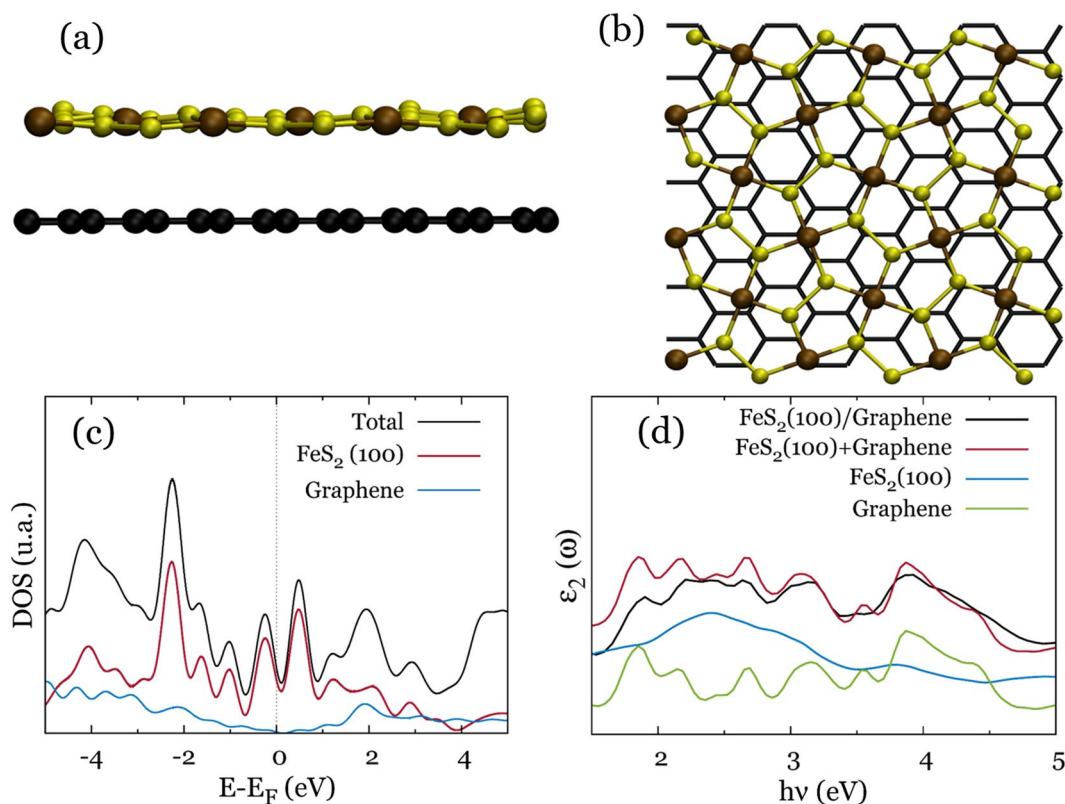
Figure 6: Main features for the $FeS_2(100)$/graphene model. (a) Side and (b) top view of the geometry. Colors: Fe, ochre; S, yellow; C, black. (c) Total and partial DOS. Fermi level is set to zero. (d) Absorption spectra including isolated fragments.

Bader charge analysis reveals that in this system there is a quite small charge transfer of only 0.021 e^-/nm^2 from the FeS_2 thin layer to the graphene sheet. This value is similar in magnitude (but of opposing sign) to that of the $Ag_2S(100)$/graphene system and is in agreement with the large (3.4 Å) minimal distance between the two components of this system.

In terms of magnetization, a greater change is observed. Fe atoms belonging to the $FeS_2(100)$/graphene system show magnetization values between $+2$ and -2 μ_B, and, thus, show an antiferromagnetic state. For the isolated $FeS_2(100)$ layer, however, a ferromagnetic arrangement is found to be the most stable, with Fe atoms showing magnetization values between $+1.88$ and $+2.58$ μ_B. This result is in agreement with the study performed by Wu and colleagues [64] where they observed that, despite the FeS_2 crystal being non-magnetic, its (100) surface shows a polarization component, being the magnetization value for the surface Fe atoms between $+2$ and $+4$ μ_B.

Total and partial DOS for this system are shown in Fig. 6c. The calculated profile shows the absence of bandgap, implying a metallic behavior. Valence and conduction bands can be projected to be a mixture of electronic states belonging to both the FeS_2 thin film and the graphene layer, with a major contribution of $FeS_2(100)$ in the electronic states closer to the Fermi level. Finally, Fig. 6d shows the absorption spectra for the $FeS_2(100)$ system as well as its isolated fragments and the sum of both independent contributions. Comparison between the calculated spectrum for the $FeS_2(100)$/system and that obtained from the addition of the isolated $FeS_2(100)$ and graphene layers shows a good correlation between both of them, which is, overall, a clear sign of an indirect electron injection mechanism.

Conclusions

We have studied the optoelectronic properties of Ag_2S/graphene and FeS_2/graphene nanostructures by means of DFT including dispersion forces. Ag_2S and FeS_2 systems were modeled as nanoclusters and nanolayers for both (100) and (010) Ag_2S surfaces and (100) FeS_2 surface. Two $(Ag_2S)_n$ NPs with $n = 4, 5$ were analyzed, showing low values of HOMO–LUMO gap and good UV–Vis optical activity. In the case of FeS_2, a single Fe_2S_4 nanocluster was selected, but was analyzed in its ferro- and antiferromagnetic states, being the antiferromagnetic the most stable and showing good optoelectronic properties. Once the isolated NPs were studied, they were adsorbed onto both graphite and graphene slab models to study the influence of the carbon inner layers. Nanocluster/graphene models show strong adsorption energy values, which guarantee the structural stability of the system as well as electron density redistribution accounting for the formation of a chemical bond between the NP and the graphene support. Bandgap values and absorption spectra obtained for these systems show high UV–Vis optical activity as well as a variety of both direct and indirect electron injection

mechanisms depending on the system. Finally, $Ag_2S(100)$, $Ag_2S(010)$ and $FeS_2(100)$ nanolayer models were adsorbed on graphene to analyzed the properties of these 2D systems. Structural stability for these thin film/graphene systems was evaluated by terms of the adsorption energy, which was found to be very similar to the graphene/graphene interaction found in graphite. Calculated absorption spectra indicate a mainly indirect electron injection mechanism and support the implementation of these materials in photovoltaic applications.

Methods

Periodic three-dimensional and spin-polarized DFT calculations were performed using the Vienna Ab initio simulation package code (VASP 5.4) [65–67] with the projector-augmented wave method, PAW [68, 69]. Energies were computed with the exchange–correlation functional proposed by Perdew et al. (PBE) [70], based on the GGA. In order to take into account the influence of the London dispersion forces, the approximation proposed by Tkatchenko and Scheffler (PBE-TS) [71] was selected. In all cases, electronic states were expanded using a plane-wave basis set with a cutoff energy of 500 eV. The silver ($5s^1 4d^{10}$), iron ($4s^1 3d^7$), sulphur ($3s^2 3p^4$) and carbon ($2s^2 2p^2$) valence electrons have been explicitly considered. A simulation cell of $20 \times 20 \times 20$ Å^3 has been employed for the Ag_2S NPs while a $15 \times 15 \times 15$ Å^3 cell was employed for the smaller FeS_2 NP. Given the size of the models considered, only Γ point was considered for all geometry optimizations and single-point electronic calculations for isolated NPs. Additionally, for single-point calculations of models involving interaction with graphite or graphene, a $4 \times 4 \times 1$ Γ-centered mesh Monkhorst–Pack set of k points was selected [72]. Wave function was considered converged when the energy difference between two consecutives SCF steps was smaller than 10^{-6} eV and 10^{-8} eV for geometry optimizations and single-point electronic calculations, respectively. Iterative relaxation of the atomic positions was stopped when forces acting on the atoms were lower than 0.01 eV/Å. Optical spectra were obtained from the imaginary part of the frequency-dependent dielectric function $\varepsilon_2(\omega)$, as proposed by Gajdoš et al. [73].

Declarations

Conflict of interest The authors declare that they have no conflict of interest.

Supplementary Information

The online version contains supplementary material available at https://doi.org/10.1557/s43578-022-00509-1.

Open Access

References

1. REN21: Renewables 2020 Global Status Report (2020)
2. W. Shockley, H.J. Queisser, J. Appl. Phys. **32**, 510 (1961). https://doi.org/10.1063/1.1736034
3. V.K. Singh, L. Giribabu, J. Innov. Electron. Commun. Eng. **3**, 44 (2013)
4. T.D. Lee, A.U. Ebong, Renew. Sustain. Energy Rev. **70**, 1286 (2017). https://doi.org/10.1016/J.RSER.2016.12.028
5. G. Conibeer, Mater. Today **10**, 42 (2007). https://doi.org/10.1016/S1369-7021(07)70278-X
6. P.V. Kamat, J. Phys. Chem. Lett. **4**, 908 (2013). https://doi.org/10.1021/jz400052e
7. J. Tian, G. Cao, Nano Rev. **4**, 22578 (2013). https://doi.org/10.3402/nano.v4i0.22578
8. M. Ye, X. Gao, X. Hong, Q. Liu, C. He, X. Liu, C. Lin, Sustain. Energy Fuels **1**, 1217 (2017). https://doi.org/10.1039/C7SE00137A
9. R.D. Schaller, V.I. Klimov, Phys. Rev. Lett. **92**, 186601 (2004). https://doi.org/10.1103/PhysRevLett.92.186601
10. S. Gorer, G. Hodes, J. Phys. Chem. **98**, 5338 (1994). https://doi.org/10.1021/j100071a026
11. I. Moreels, K. Lambert, D. De Muynck, F. Vanhaecke, D. Poelman, J.C. Martins, G. Allan, Z. Hens, Chem. Mater. **19**, 6101 (2007). https://doi.org/10.1021/cm071410q
12. I.L. Medintz, M.H. Stewart, S.A. Trammell, K. Susumu, J.B. Delehanty, B.C. Mei, J.S. Melinger, J.B. Blanco-Canosa, P.E. Dawson, H. Mattoussi, Nat. Mater. **9**, 676 (2010). https://doi.org/10.1038/nmat2811
13. I.L. Medintz, D. Farrell, K. Susumu, S.A. Trammell, J.R. Deschamps, F.M. Brunel, P.E. Dawson, H. Mattoussi, Anal. Chem. **81**, 4831 (2009). https://doi.org/10.1021/ac900412j
14. D. Loss, D.P. DiVincenzo, Phys. Rev. A **57**, 120 (1998). https://doi.org/10.1103/PhysRevA.57.120
15. J.J. Coleman, J.D. Young, A. Garg, J. Light Technol. **29**, 499 (2011). https://doi.org/10.1109/JLT.2010.2098849
16. E. Jang, S. Jun, H. Jang, J. Lim, B. Kim, Y. Kim, Adv. Mater. **22**, 3076 (2010). https://doi.org/10.1002/adma.201000525
17. R. Brendel, J.H. Werner, H.J. Queisser, Sol. Energy Mater. Sol. Cells **41–42**, 419 (1996). https://doi.org/10.1016/0927-0248(95)00125-5
18. S. Park, R.S. Ruoff, Nat. Nanotechnol. **4**, 217 (2009). https://doi.org/10.1038/nnano.2009.58
19. J. Wu, W. Pisula, K. Müllen, Chem. Rev. **107**, 718 (2007). https://doi.org/10.1021/CR068010R
20. F. Chen, N.J. Tao, Acc. Chem. Res. **42**, 429 (2009). https://doi.org/10.1021/ar800199a
21. D.R. Dreyer, S. Park, C.W. Bielawski, R.S. Ruoff, Chem. Soc. Rev. **39**, 228 (2010). https://doi.org/10.1039/B917103G
22. C.A. Ubani, M.A. Ibrahim, M.A.M. Teridi, K. Sopian, J. Ali, K.T. Chaudhary, Sol. Energy **137**, 531 (2016). https://doi.org/10.1016/J.SOLENER.2016.08.055
23. X. Zeng, X. Xiao, W. Zhang, C. Wan, H. Wang, Comput. Mater. Sci. **126**, 43 (2017). https://doi.org/10.1016/J.COMMATSCI.2016.09.014
24. N.S. Mikhaleva, M.A. Visotin, A.A. Kuzubov, Z.I. Popov, J. Phys. Chem. C **121**, 24179 (2017). https://doi.org/10.1021/acs.jpcc.7b07630
25. C.X. Guo, H.B. Yang, Z.M. Sheng, Z.S. Lu, Q.L. Song, C.M. Li, Angew. Chem. Int. Ed. **49**, 3014 (2010). https://doi.org/10.1002/anie.200906291
26. E. Bi, Y. Su, H. Chen, X. Yang, M. Yin, F. Ye, Z. Li, L. Han, RSC Adv. **5**, 9075 (2015). https://doi.org/10.1039/C4RA14029J
27. Z.J. Li, B.C. Yang, X.W. Lv, Y.C. Li, L. Wang, Appl. Surf. Sci. **370**, 508 (2016). https://doi.org/10.1016/J.APSUSC.2015.12.053
28. Q. Xiang, J. Yu, J. Phys. Chem. Lett. **4**, 753 (2013). https://doi.org/10.1021/jz302048d
29. A. Martí, G.L. Araújo, Sol. Energy Mater. Sol. Cells **43**, 203 (1996). https://doi.org/10.1016/0927-0248(96)00015-3
30. A. Tubtimtae, K. Wu, H.-Y. Tung, M.-W. Lee, G.J. Wang, Electrochem. Commun. **12**, 1158 (2010). https://doi.org/10.1016/J.ELECOM.2010.06.006
31. J.A. Suárez, J.J. Plata, A.M. Márquez, J.F. Sanz, Theor. Chem. Acc. **135**, 70 (2016). https://doi.org/10.1007/s00214-016-1832-x

32. J. Amaya Suárez, J.J. Plata, A.M. Márquez, J. Fernández Sanz, J. Phys. Chem. A **121**, 7290 (2017). https://doi.org/10.1021/acs.jpca.7b07731

33. M. Wang, Y. Wang, A. Tang, X. Li, Y. Hou, F. Teng, Mater. Lett. **88**, 108 (2012). https://doi.org/10.1016/j.matlet.2012.08.027

34. Y. Zhang, Y. Liu, C. Li, X. Chen, Q. Wang, J. Phys. Chem. C **118**, 4918 (2014). https://doi.org/10.1021/jp501266d

35. P.P. Altermatt, T. Kiesewetter, K. Ellmer, H. Tributsch, Sol. Energy Mater. Sol. Cells **71**, 181 (2002). https://doi.org/10.1016/S0927-0248(01)00053-8

36. A. Ennaoui, H. Tributsch, Sol. Cells **13**, 197 (1984). https://doi.org/10.1016/0379-6787(84)90009-7

37. A.S. Aricò, V. Antonucci, P.L. Antonucci, E. Modica, S. Ferrara, N. Giordano, Mater. Lett. **13**, 12 (1992). https://doi.org/10.1016/0167-577X(92)90169-K

38. A. Ennaoui, H. Tributsch, Sol. Energy Mater. **14**, 461 (1986). https://doi.org/10.1016/0165-1633(86)90030-4

39. A. Ennaoui, S. Fiechter, H. Tributsch, M. Giersig, R. Vogel, H. Weller, J. Electrochem. Soc. **139**, 2514 (1992). https://doi.org/10.1149/1.2221255

40. E.K. Li, K.H. Johnson, D.E. Eastman, J.L. Freeouf, Phys. Rev. Lett. **32**, 470 (1974). https://doi.org/10.1103/PhysRevLett.32.470

41. J.F.W. Mosselmans, R.A.D. Pattrick, G. van der Laan, J.M. Charnock, D.J. Vaughan, C.M.B. Henderson, C.D. Garner, Phys. Chem. Miner. **22**, 311 (1995). https://doi.org/10.1007/BF00202771

42. A. Fujimori, K. Mamiya, T. Mizokawa, T. Miyadai, Phys. Rev. B **54**, 16329 (1996). https://doi.org/10.1103/PhysRevB.54.16329

43. H.W. Nesbitt, A.G. Berlich, S.L. Harmer, I. Uhlig, G.M. Bancroft, R. Szargan, Am. Mineral. **89**, 382 (2004). https://doi.org/10.2138/am-2004-2-319

44. K.C. Prince, M. Matteucci, K. Kuepper, S.G. Chiuzbaian, S. Bartkowski, M. Neumann, Phys. Rev. B **71**, 085102 (2005). https://doi.org/10.1103/PhysRevB.71.085102

45. K.M. Rosso, U. Becker, M.F. Hochella, Am. Mineral. **84**, 1535 (1999). https://doi.org/10.2138/am-1999-1007

46. T.A. Bither, R.J. Bouchard, W.H. Cloud, P.C. Donohue, W.J. Siemons, Inorg. Chem. **7**, 2208 (1968). https://doi.org/10.1021/ic50069a008

47. W. Folkerts, G.A. Sawatzky, C. Haas, R.A. De Groot, F.U. Hillebrecht, J. Phys. C **20**, 4135 (1987). https://doi.org/10.1088/0022-3719/20/26/015

48. P. Raybaud, J. Hafner, G. Kresse, H. Toulhoat, J. Phys. Condens. Matter **9**, 11107 (1997). https://doi.org/10.1088/0953-8984/9/50/014

49. V. Eyert, K. Höck, Phys. Rev. B **57**, 6350 (1998). https://doi.org/10.1103/PhysRevB.57.6350

50. G.U. Von Oertzen, W.M. Skinner, H.W. Nesbitt, Phys. Rev. B **72**, 235427 (2005). https://doi.org/10.1103/PhysRevB.72.235427

51. D.W. Wang, Q.H. Wang, T.M. Wang, CrystEngComm **12**, 755 (2010). https://doi.org/10.1039/b917941k

52. Y. Bi, Y. Yuan, C.L. Exstrom, S.A. Darveau, J. Huang, Nano Lett. **11**, 4953 (2011). https://doi.org/10.1021/nl202902z

53. W. Li, M. Döblinger, A. Vaneski, A.L. Rogach, F. Jäckel, J. Feldmann, J. Mater. Chem. **21**, 17946 (2011). https://doi.org/10.1039/c1jm13336e

54. T.J. Whittles, T.D. Veal, C.N. Savory, A.W. Welch, F.W. de Souza Lucas, J.T. Gibbon, M. Birkett, R.J. Potter, D.O. Scanlon, A. Zakutayev, V.R. Dhanak, ACS Appl. Mater. Interfaces **9**, 41916 (2017). https://doi.org/10.1021/acsami.7b14208

55. A.R. Jang, J.E. Lim, S. Jang, M.H. Kang, G. Lee, H. Chang, E.K. Kim, J.K. Park, J.O. Lee, Appl. Surf. Sci. **562**, 150201 (2021). https://doi.org/10.1016/J.APSUSC.2021.150201

56. Z. Mo, P. Liu, R. Guo, Z. Deng, Y. Zhao, Y. Sun, Mater. Lett. **68**, 416 (2012). https://doi.org/10.1016/J.MATLET.2011.11.006

57. B. Kilic, S. Turkdogan, O.C. Ozer, M. Asgin, O. Bayrakli, G. Surucu, A. Astam, D. Ekinci, Mater. Lett. **185**, 584 (2016). https://doi.org/10.1016/J.MATLET.2016.06.069

58. X. He, Y. Wang, C.Y. Gao, H. Jiang, L. Zhao, Chem. Sci. **6**, 654 (2015). https://doi.org/10.1039/c4sc01884b

59. R. Sánchez-de-Armas, J. Oviedo, M.A. San Miguel, J.F. Sanz, J. Phys. Chem. C **115**, 11293 (2011). https://doi.org/10.1021/jp201233y

60. R. Sánchez-de-Armas, M.A. San-Miguel, J. Oviedo, J.F. Sanz, Comput. Theor. Chem. **975**, 99 (2011). https://doi.org/10.1016/J.COMPTC.2011.01.010

61. J.A. Suárez, J.J. Plata, A.M. Márquez, J.F. Sanz, Phys. Chem. Chem. Phys. **19**, 14580 (2017). https://doi.org/10.1039/C7CP01076A

62. N.H. De Leeuw, S.C. Parker, H.M. Sithole, P.E. Ngoepe, J. Phys. Chem. B **104**, 7969 (2000). https://doi.org/10.1021/jp0009498

63. D.R. Alfonso, J. Phys. Chem. C **114**, 8971 (2010). https://doi.org/10.1021/jp100578n

64. Y.N. Zhang, J. Hu, M. Law, R.Q. Wu, Phys. Rev. B **85**, 85314 (2012). https://doi.org/10.1103/PhysRevB.85.085314

65. G. Kresse, J. Furthmüller, Phys. Rev. B **54**, 11169 (1996). https://doi.org/10.1103/PhysRevB.54.11169

66. G. Kresse, J. Furthmüller, Comput. Mater. Sci. **6**, 15 (1996). https://doi.org/10.1016/0927-0256(96)00008-0

67. G. Kresse, J. Hafner, Phys. Rev. B **47**, 558 (1993). https://doi.org/10.1103/PhysRevB.47.558

68. P.E. Blöchl, Phys. Rev. B **50**, 17953 (1994). https://doi.org/10.1103/PhysRevB.50.17953

69. G. Kresse, D. Joubert, Phys. Rev. B **59**, 1758 (1999). https://doi.org/10.1103/PhysRevB.59.1758

70. J.P. Perdew, K. Burke, M. Ernzerhof, Phys. Rev. Lett. **77**, 3865 (1996). https://doi.org/10.1103/PhysRevLett.77.3865

71. A. Tkatchenko, M. Scheffler, Phys. Rev. Lett. **102**, 073005 (2009). https://doi.org/10.1103/PhysRevLett.102.073005

72. H.J. Monkhorst, J.D. Pack, Phys. Rev. B **13**, 5188 (1976). https://doi.org/10.1103/PhysRevB.13.5188

73. M. Gajdoš, K. Hummer, G. Kresse, J. Furthmüller, F. Bechstedt, Phys. Rev. B **73**, 045112 (2006). https://doi.org/10.1103/PhysRevB.73.045112